Journal of Alloys and Compounds 508 (2010) 119–128

Contents lists available at ScienceDirect

Journal of Alloys and Compounds

journal homepage: www.elsevier.com/locate/jallcom

Catalytic effects of nano-sized TiC additions on the hydrogen storage properties of $LiAlH_4$

Rafi-ud-din*, Lin Zhang, Li Ping, Qu Xuanhui

State Key Laboratory for Advanced Metals and Materials, School of Materials Science and Engineering, USTB, Beijing 100083, China

ARTICLE INFO

Article history:
Received 12 May 2010
Received in revised form 30 July 2010
Accepted 4 August 2010
Available online 11 August 2010

Keywords:
Hydrogen storage materials
Complex hydrides
Lithium alanate ($LiAlH_4$)
Nanocatalyst doping
Mechanical (ball) milling
Nano-sized TiC
Desorption temperature and kinetics
Differential scanning calorimetry (DSC)

ABSTRACT

The catalytic effect of TiC nanopowder addition in varying proportions on the hydrogen storage properties of $LiAlH_4$ has been investigated by pressure-composition-temperature (PCT) experiments, thermogravimetry (TG), and differential scanning calorimetry (DSC). The results indicate that doped samples are able to dehydrogenate at much lower temperatures; for example, the onset of dehydrogenation is 85 °C for $LiAlH_4$–2 mol% TiC, and the majority of hydrogen (~6.9 wt.%) can be released by 188 °C. About 5 out of 6.9 wt.% of H_2 can be released in the range of 85–138 °C (heating rate 4 °C min^{-1}). Isothermal desorption results at 115 °C reveal that doped alanate exhibits dehydriding rate 7–8 times faster than that of pure $LiAlH_4$. DSC measurements indicate that enthalpies of decomposition in $LiAlH_4$ decrease significantly with doping. From Kissinger analysis, the apparent activation energies are estimated to be 59 kJ/mol, 70 kJ/mol and 99 kJ/mol for the decompositions of $LiAlH_4$, Li_3AlH_6 and LiH, respectively. The results of first rehydrogenation indicate that 5 mol% dopant exhibits the maximum absorption of about 1.9 wt.%. XRD, FESEM, EDS, FTIR, and XPS analyses are utilized to put forward a possible catalytic mechanism of nano-sized TiC in ameliorating the dehydriding/rehydriding characteristics of doped $LiAlH_4$.

1. Introduction

The major obstacle to the transition from a carbon-based/fossil fuel energy system to a hydrogen-based economy is the identification of efficient and cost-effective means for on-board storage of hydrogen. Despite the decades of intense research efforts, so far none of the materials has satisfied the performance targets specified by automotive industry with respect to gravimetric density, hydrogenation/dehydrogenation kinetics, and thermodynamic properties. Recently, complex hydrides such as alanates (AlH_4^-), amides (NH_2^-), and borohydrides (BH_4^-) have attracted considerable attention, as they inevitably provide extremely high gravimetric storage capacities compared to that of conventional metal hydrides [1–14]. But, the practical utility of most of these complex hydrides is limited by their poor kinetics and difficulty in reversing the hydrogen under the moderate conditions. Alanates of the general form $MAlH_4$, where M is a light weight alkaline metal (Li, Na or K), have a high gravimetric density of hydrogen, which is essential for their potential use as hydrogen storage materials. Following the breakthrough work on Ti-doped $NaAlH_4$ [15], lithium alanates ($LiAlH_4$) as well as alanates of other alkali-and alkaline-earth-metal-based complex aluminum hydrides have received a great deal of attention as possible candidate materials because of their light weight and high inherent storage capacity [16,17]. Among the alanates, the hydrogen content of two alkali metal aluminohydrides, $LiAlH_4$ and $NaAlH_4$, are 10.5 wt.% and 7.3 wt.% H_2, respectively. However, the relatively low hydrogen content of sodium aluminohydrides (5.6 wt.% H when $NaAlH_4$ decomposes to NaH, Al and H_2) renders them inferior to other hydrides such as lithium aluminohydrides (7.9 wt.% H when $LiAlH_4$ decomposed to LiH, Al and H_2) and magnesium hydride (7.6 wt.% H_2). Upon heating, the decomposition of $LiAlH_4$ takes place in three steps [1] with 5.3 wt.%, 2.6 wt.% and 2.6 wt.% release of hydrogen, respectively.

$$3LiAlH_4 \rightarrow Li_3AlH_6 + 2Al + 3H_2 \quad (1)$$

$$Li_3AlH_6 + 2Al \rightarrow 3LiH + 3Al + 3/2H_2 \quad (2)$$

$$3LiH + 3Al \rightarrow 3LiAl + 3/2H_2 \quad (3)$$

Reaction (3) occurs above 400 °C and is not considered viable for practical purposes. The decomposition temperature ranges for reactions (1) and (2) are 150–175 °C and 180–220 °C, respectively [1].

Lithium alanate ($LiAlH_4$) hydrid indeed exhibits among the highest hydrogen capacity, but its high capacity is plagued by some of its drawbacks such as the presence of exothermic decomposition reaction, extremely high plateau pressure at relatively low

* Corresponding author. Tel.: +86 10 62332700; fax: +86 10 62334311.
E-mail address: rafi.682@yahoo.com (Rafi-ud-din).

0925-8388/$ – see front matter © 2010 Elsevier B.V. All rights reserved.
doi:10.1016/j.jallcom.2010.08.008

temperatures which makes the hydride practically irreversible and relatively slow hydrogen desorption kinetics. Recent studies have indicated that both ball-milling and doping with various catalysts have not only rendered the low-temperature decomposition of lithium aluminohydride into lithium hexahydroaluminate, aluminum, and hydrogen but also to some extent has caused the partial reversibility of reaction (2) by eliminating the kinetic restrictions. It is documented that by using TiF_3 [18], Ce $(So_4)_2$ [19,20], $TiCl_3$ [21], $TiCl_3$. (1/3)$(AlCl_3)$ [22,23], $LaCl_3$ [20,24], VBr_3 [25], Ni [19,20], Fe [26], Ti, Sc, V [20,26,27], $NiCl_2$ [28], NbF_5 [29], VCl_3, and carbon nanofibers [30], a significant reduction in the decomposition temperatures of the first and the second steps can be achieved. In addition, partial reversibility of reaction (2) has been claimed by $LaCl_3$ [20,24], Ni [19,20], Ti [20], Ce $(SO_4)_2$ [19,20], VCl_3 [30], carbon nanofibers [30], and $TiCl_3$ [23]. However, the most of these catalysts induce the reduction in hydrogen storage capacity during the ball-milling. Therefore, there have been persistent efforts to find new effective catalysts that can enhance the reaction kinetics while maintaining the high hydrogen capacity.

Tailoring nanophase structure by using foreign scaffolds is found to dramatically improve kinetics and thermodynamics of hydrogen exchange reactions of the complex hydride materials. The nanostructured catalytic dopants may offer several advantages for the physicochemical reactions such as surface interactions, adsorption in addition to bulk absorption, rapid kinetics, low-temperature sorption, hydrogen atom dissociation, and molecular diffusion via the surface catalyst [31–34]. TiC is well known for its high degree of hardness and stability due to its high Ti–C bond enthalpy. Recently, Xuezhang et al. [35] have reported the role of TiC as a catalyst in the improvement of hydriding/dehydriding properties of the sodium alanate. In the present work, the efficacy of TiC nanoparticles is evaluated by subjecting the doped samples to the dehydrogenation and rehydrogenation experiments by pressure-composition-temperature (PCT) apparatus, thermogravimetry (TG), and differential scanning calorimetry (DSC). TiC nanopowder, in varying proportions, has been incorporated into $LiAlH_4$ by high-energy ball-milling.

2. Experimental details

$LiAlH_4$ (≥95%, average 325 mesh) and TiC (≥99%, <30 nm) were purchased from Sigma–Aldrich Co. and Hefei Kaier Development Co., Ltd. (China), respectively. Both the materials were used as-received without any further purification. All material handlings (including weighing and loading) were performed in high purity argon filled glove box, with low oxygen and water vapour content. $LiAlH_4$ (typically 1–2 g) was mixed with 1 mol%, 2 mol%, 3 mol%, 4 mol% and 5 mol% TiC and ball-milled for 30 min by using a high-energy Spex mill. All the samples were loaded into the hardened steel vial under an argon atmosphere in a glove box. Steel balls (1 g and 3 g) were added with a ball to powder weight ratio of 15:1. Air-cooling of the vial was employed to prevent its heating during the ball-milling process.

Hydriding/dehydriding properties of the as-received and doped samples were investigated by using a pressure-composition-temperature (PCT) apparatus. The details of apparatus are given in our previous report [36]. The apparatus can be operated up to the maximum pressure of 10 MPa and 600 °C. About 0.5 g of sample was loaded into the sample vessel. For dehydrogenation (first two steps) measurements, the samples of $LiAlH_4$ doped with 1 mol%, 2 mol%, 3 mol%, 4 mol% and 5 mol% TiC were heated up to 250 °C at a heating rate of 4 °C min^{-1} under a controlled vacuum atmosphere. During the heating process, all the temperature and pressure data were documented and the curves for the two-stage process were drawn by using computer software. Following the first complete dehydrogenation (first two steps), the samples were subjected to rehydrogenation studies at 165 °C under 9.5 MPa for 3 h. The pressure drop with time in the closed system testified the rehydrogenation of the samples. Subsequently, the rehydrogenated samples were dehydrogenated at similar temperature.

The simultaneous DSC and TG analyses were conducted by using NETZSCH STA 449C. All measurements were carried out under a flow (50 ml min^{-1}) of high purity argon (99.999%). Sample mass was typically 5 mg. Heating runs were performed at different rates (4 °C min^{-1}, 7 °C min^{-1} and 10 °C min^{-1}) from 35 °C to 500 °C.

The phase structure of the sample following the ball-milling, dehydrogenation, and rehydrogenation was determined by a MXP21VAHF X-ray diffractometer (XRD with CuKα radiation) at room temperature. XRD was done at a tube voltage of 40 kV and a tube current of 200 mA. The X-ray intensity was measured over a diffraction angle from 10° to 90° with a velocity of 0.02° per step. The samples were covered with the liquid paraffin to prevent the oxidation during the XRD test.

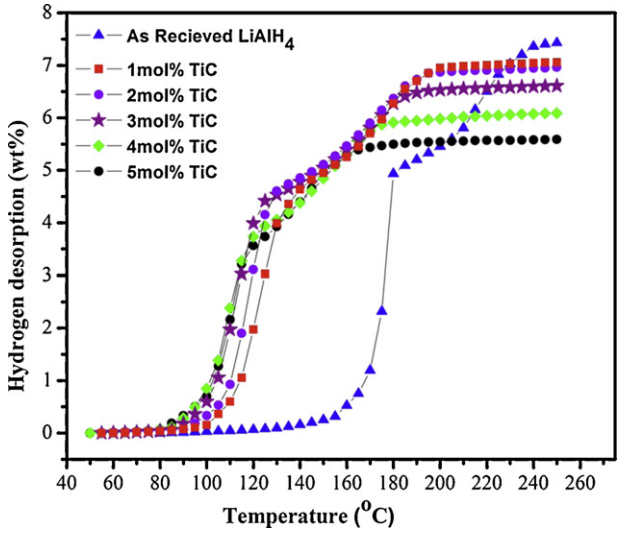

Fig. 1. Thermal desorption profiles of as-received $LiAlH_4$ and $LiAlH_4$ doped with 1 mol%, 2 mol%, 3 mol%, 4 mol%, and 5 mol% TiC. The samples are heated up to 250 °C at the heating rate of 4 °C min^{-1}.

FTIR spectroscopy was performed by using an infrared spectrophotometer (NEXUS670). The spectral resolution was 4 cm^{-1}. Scans were done between 2000 cm^{-1} and 800 cm^{-1} under an argon atmosphere. X-ray photoelectron spectroscopy (XPS) was performed with a PHI-5300 XPS spectrometer.

The as-received, doped, and dehydrogenated samples were examined by a field emission scanning electron microscope (FESEM-6301F) coupled with energy dispersive spectroscopy (EDS). Sample preparation for the FESEM measurement was carried out inside the glove box and, moreover, the samples were transferred to the SEM chamber by means of a device maintaining an Ar overpressure.

3. Results and discussion

Fig. 1 exhibits the non-isothermal dehydrogenation performances of the as-received $LiAlH_4$, and the $LiAlH_4$ doped with 1 mol%, 2 mol%, 3 mol%, 4 mol%, and 5 mol% TiC nanopowders. The desorption curves clearly depict that the $LiAlH_4$ samples balled milled with nano-sized TiC have rendered quite striking effects not only on the dehydrogenation characteristics of the first reaction (1) but also on the second reaction (2). Obviously, the onset temperature of dehydrogenation for all the Li alanate/carbide composite samples is below 100 °C, a significant reduction compared with neat $LiAlH_4$, in which dehydrogenation starts at around 150 °C. The pure $LiAlH_4$ starts to decompose at around 150 °C for the first stage and desorbs about 4.9 wt.% hydrogen. In the second stage, it initiates to dehydrogenate at 180 °C, and about 2.5 wt.% hydrogen is released. Hence the total dehydriding capacity of pure alanate is about 7.4 wt.%. $LiAlH_4$ with 1 mol% TiC releases about 6.96 wt.% hydrogen in a desorption temperature range between 100 °C and 200 °C. The addition of 2–3 mol% TiC nanopowders further reduces the first decomposition temperature of $LiAlH_4$ by the factor of around 60–65 °C, and the second decomposition temperature by the factor of around 50–55 °C, respectively. The sample of 2 mol% dopant initiates to decompose at 90 °C and terminates at 130 °C for the first stage, whilst the sample with 3 mol% dopant starts the decomposition at 85 °C and concludes at 125 °C. The second stage of the decomposition of 2 mol% and 3 mol% samples terminates at 190 °C and 185 °C, respectively. The hydrogen release contents in the first and second steps, for the sample doped with 2 mol%, are 4.60 wt.% and 2.25 wt.%, respectively. However, the desorption capacity with 3 mol% addition degrades, and amounts to 4.41 wt.% and 2.06 wt.% in the first and second stages, respectively. Further raising the doping amount to 5 mol% shortens the desorp-

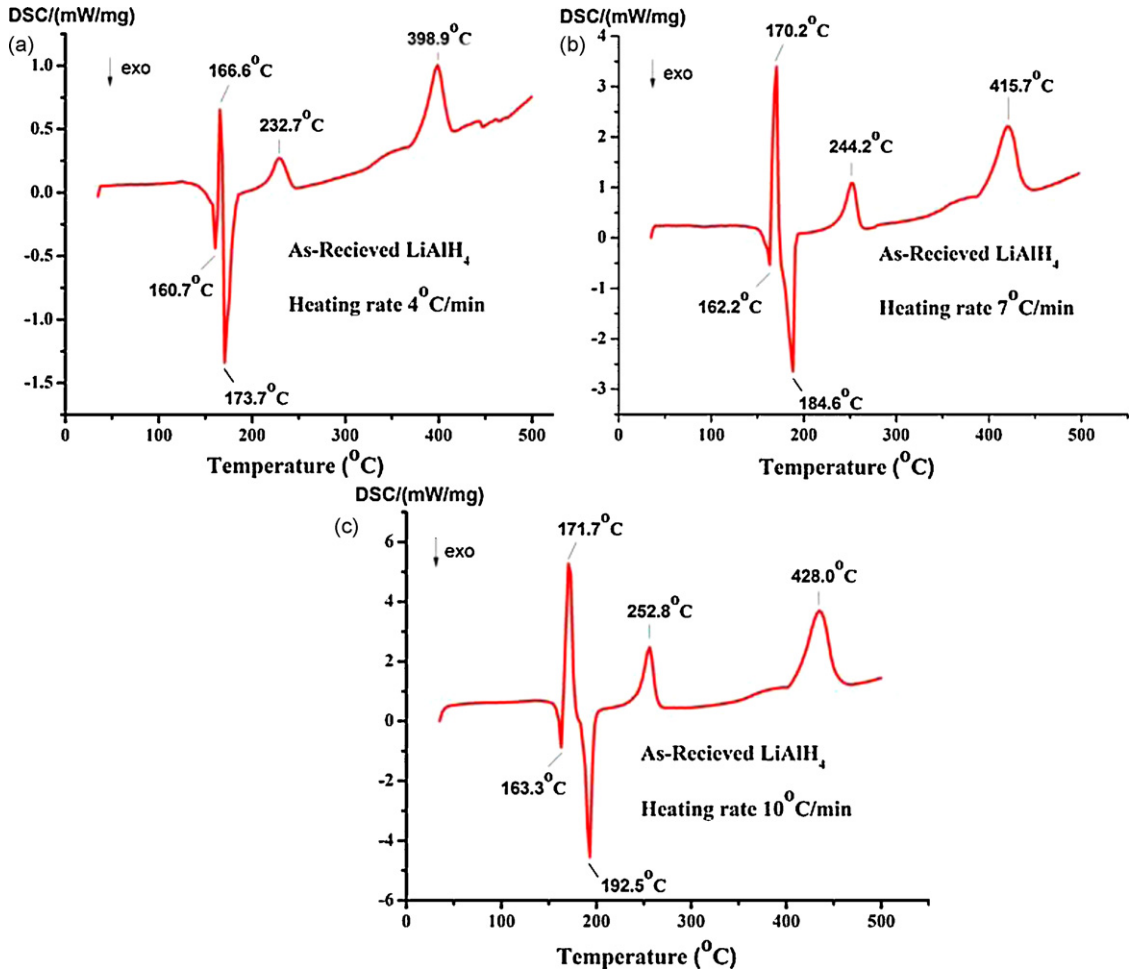

Fig. 2. DSC profiles of as-received $LiAlH_4$ within the temperature range of 35–500 °C at the heating rates of (a) 4 °C min^{-1}, (b) 7 °C min^{-1}, and (c) 10 °C min^{-1}.

tion temperature range to 80–170 °C but with the cost of more loss of hydrogen release content. The overall hydrogen release content with 5 mol% sample is 5.43 wt.%, which is about 74% of the total amount of hydrogen released by the pure $LiAlH_4$. The decrease in the maximum capacity may be associated with the impurity in the original $LiAlH_4$ powder, the amount of dopant, and some partial decomposition of $LiAlH_4$ during high-energy ball-milling with very hard and brittle nano-sized TiC. Despite the air-cooling of the vial employed during the milling process, the localized impact associated with the ball-milling induces the localized temperature increase of the alanate powders being ball-milled and heavily catalyzed with TiC nanoparticles. We assume that the simultaneous effect of both the temperature increase during milling and catalyst causes the partial decomposition of alanate. For the small additions, the loss in capacity is insignificant owing to the moderate exposure of alanate to the catalyst. However, it is noted that doped alanate eventually releases hydrogen as much as 6.96 wt.%, which is quite large compared to the hydrogen capacity of $LiAlH_4$ with various catalysts reported in the literature [18–21,23,24,26,27,30,37]. By considering that large amount of dopant is detrimental in terms of gravimetrical hydrogen density, the 2 mol% doping amount can be considered a best compromise between the dehydrogenation rate and the hydrogen yield.

Figs. 2 and 3 demonstrate the results of TG/DSC experiments performed with the samples of undoped $LiAlH_4$ and $LiAlH_4$ doped with 2 mol% TiC nanopowder. The TG/DSC profiles are measured within the temperature range of 35–500 °C at various heating rates (4 °C min^{-1}, 7 °C min^{-1} and 10 °C min^{-1}, respectively). Fig. 2 illustrates the DSC results of the as-received $LiAlH_4$. It is clear that for the as-received $LiAlH_4$, there are two peaks corresponding to exothermic processes and three peaks corresponding to endothermic processes. The first exothermic peak around at 160–163 °C may be assigned to the interaction of $LiAlH_4$ with surface hydroxyl impurities, and the first endothermic peak at 166–172 °C corresponds to the melting of $LiAlH_4$. The second exothermic peak at 173–192 °C corresponds to the decomposition of liquid $LiAlH_4$ (first reaction stage), and the second endothermic peak at 232–253 °C is assigned to the decomposition of Li_3AlH_6 (second reaction stage). The third endothermic peak at 398–428 °C is ascribed to the decomposition of LiH (third reaction stage). With doping of TiC, the number of thermal events is reduced from five to only three. The one exothermic and two endothermic peaks of the DSC profiles, in Fig. 3, correspond to the three hydrogen desorption steps in reactions (1), (2), and (3), respectively. The resulting peak temperatures, measured in Fig. 3(a), are quite small compared to that of pure and catalyzed Li alanate documented in the previous reports [18,23,29,38]. The TG curve in Fig. 3(a) presents a signal of an obvious weight loss of about 6.91 wt.% in a desorption temperature range between 85 °C and 188 °C. These results are in good agreement with that obtained from the determined dehydriding capacity of the 2 mol% additions in Fig. 1. Fig. 3(a) indicates that the dehydrogenation begins at 85 °C and about 5 wt.% H_2 is released with the temperature going up to 138 °C. The time interval is only 12 min. Thereby, the dehydrogenation is very rapid under moderate temperature. The DSC curves are analyzed by the NETZSCH thermal analysis software. First, the onset and end temperatures of the peak are determined. Then, the peak

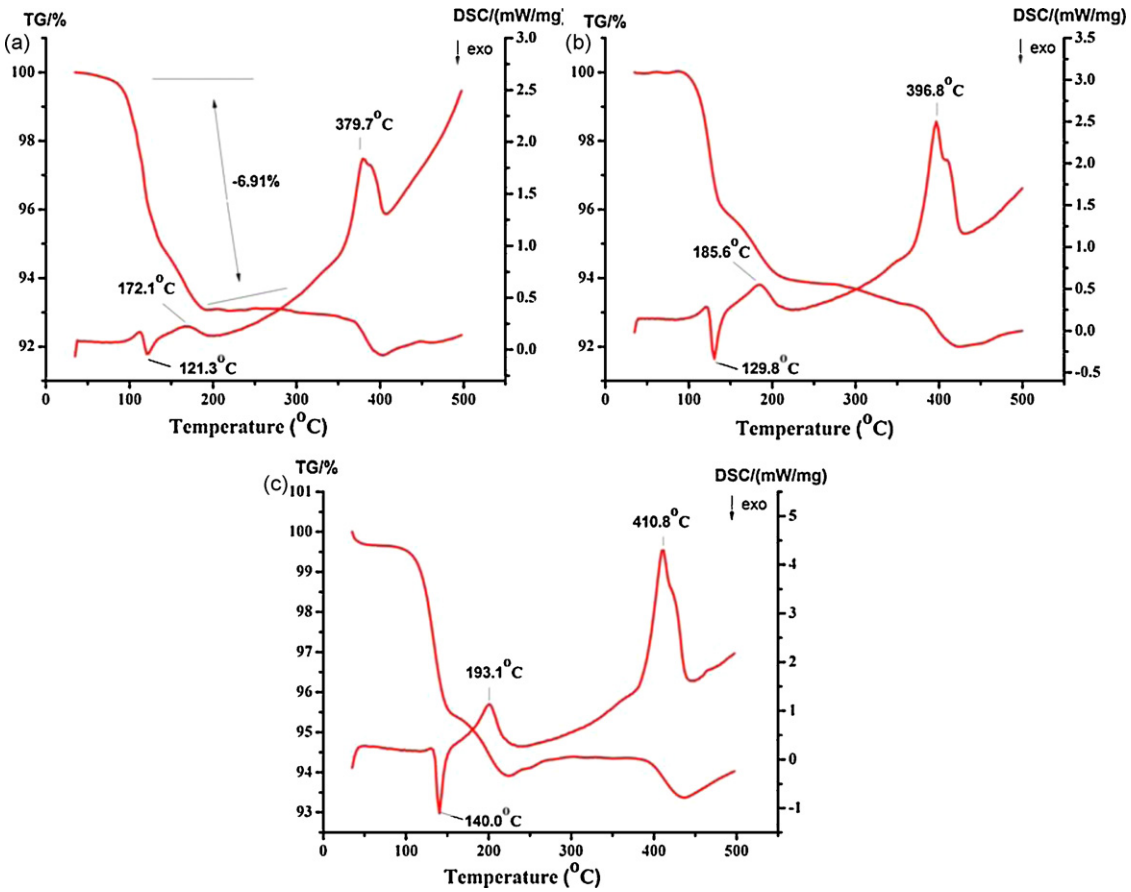

Fig. 3. TG/DSC profiles of $LiAlH_4$ +2 mol% TiC within the temperature range of 35–500 °C at the heating rates of (a) 4 °C min^{-1}, (b) 7 °C min^{-1}, and (c) 10 °C min^{-1}.

area is calculated by using the linear approach from the onset temperature to the end temperature by the DSC software. From the peak areas, the decomposition enthalpies of undoped and doped sample are determined. For the as-received sample, the reaction enthalpies of first two decompositions are -10.3 ± 0.05 kJ/mol and 9.7 ± 0.07 kJ/mol, respectively. Table 1 compares the desorption enthalpies determined in the present work to those of previously reported ones. The desorption enthalpies of the doped samples, for the first and second stages, are determined to be -2.5 ± 0.09 kJ/mol and 4.7 ± 0.16 kJ/mol, respectively. These values indicate that the dehydrogenation enthalpy for exothermic reaction increases and for endothermic reaction decreases compared with that of pure $LiAlH_4$ [39–41], which verifies the destabilization of $LiAlH_4$ by TiC nanoparticles. Hence, the improved dehydriding properties of the doped alanate can be attributed to a favorable thermodynamic modification, namely the change of enthalpy here.

By performing the Kissinger's analysis [42], i.e., an analysis of the sensitivity of the peak positions, in terms of T, the temperature of the peak maximum, to the applied heating rate, β, the apparent activation energy, E_A, can be obtained from the equation

$$\frac{d\ \ln(\beta/T^2)}{d(1/T)} = -\frac{E_A}{R} \tag{4}$$

The apparent activation energy E_A can be estimated from the slope of the plot of $\ln(\beta/T^2)$ vs. $1000/T$. The calculated apparent activation energies, E_A, for the first, second, and third decomposition steps for the pure alanate are 86 kJ/mol, 101 kJ/mol, and 138 kJ/mol, respectively. It is evident in Table 1 that the value of activation energy for first stage obtained in our work compares very well with that reported by Andreasen [38,43]. For second stage, our present value of 101 kJ/mol compares favorably with nearly all the literature reported values except 153 kJ/mol in [44] and 86 kJ/mol in

Table 1
Activation energies and decomposition enthalpies of pure $LiAlH_4$.

Parameter	Way of determination	First Stage	Second Stage	References
Activation energy (kJ/mol)	Kissinger method	122	153	[44]
	Isothermal	99.6	100	[45]
	Desorption curve fitting	82	90	[43]
	Kissinger method	115	86	[39]
	Kissinger method	86	101	This work
	Kissinger method	81	108	[38]
	Isothermal	111	100	[46]
Decomposition enthalpy (kJ/mol)	Experimental	−14	15	[39]
	Theoretical	9.79	15.72	[41]
	Experimental	−10	–	[40]
	Experimental	−10.3	9.7	This work

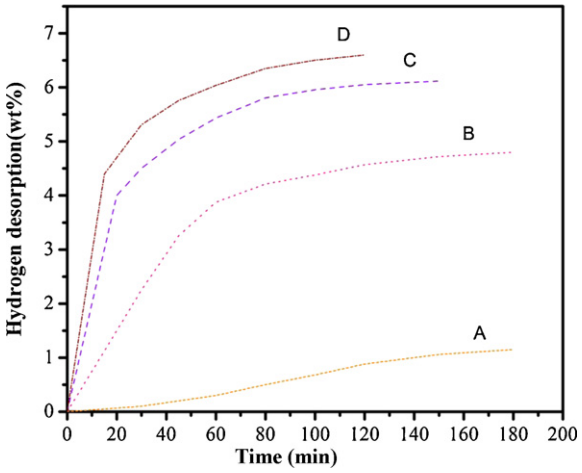

Fig. 4. Isothermal dehydrogenation kinetics of (A) as-received $LiAlH_4$ at 115 °C and the $LiAlH_4$ + 2 mol% TiC at (B) 100 °C, (C) 115 °C, and (D) 125 °C.

[39,44]. The derived apparent activation energies, E_A, for the doped samples for the first, second, and third decomposition reactions are 59 kJ/mol, 70 kJ/mol, and 99 kJ/mol, respectively. These values are slightly higher than that reported for $LiAlH_4$ doped with $TiCl_3{\cdot}1/3AlCl_3$ [23] and carbon nanofibre (CNF) [30] but smaller than that reported for NbF_5 and Ti-doped $LiAlH_4$ [29,38]. Andreasen [38] have shown that the doping of $TiCl_3$ to $LiAlH_4$ exhibits no variation in the apparent activation energy of undoped Li alanate. On the contrary, TiC has displayed a significant effect on the decomposition kinetics of Li alanate. This discrepancy between TiC and $TiCl_3$ may be attributed to the difference in their catalytic mechanisms.

The isothermal dehydrogenation kinetic curves of composite materials based on lithium aluminium hydride ball-milled with 2 mol% nano TiC powder, at different temperatures, are shown in Fig. 4. For comparison the dehydrogenation kinetics of pure $LiAlH_4$, decomposed at 115 °C, is also included. The dehydriding rates of the doped sample increase noticeably with increasing the dehydriding temperature. Within 2 h, the dehydriding capacities of the $LiAlH_4$/TiC composite at 100 °C, 115 °C, and 125 °C are 4.6 wt.%, 6.05 wt.%, and 6.6 wt.%, respectively. It is evident that pristine $LiAlH_4$ exhibits the poor kinetics. The dehydrogenation kinetics improves considerably by the addition of titanium carbide nanopowder. The TiC-doped sample shows an average dehydriding rate 7–8 times faster than that of neat $LiAlH_4$.

Table 2
Kinetic models examined for the isothermal dehydrogenation curves of TiC-doped $LiAlH_4$ at 100 °C, 115 °C and 125 °C.

Symbol	Reaction model description	Integral $f(\alpha)$ form
D1	1D diffusion	α^2
D2	2D diffusion	$\alpha + (1-\alpha)\ln(1-\alpha)$
D3	Jander equation for 3D diffusion	$[1-(1-\alpha)^{1/3}]^2$
D4	3D diffusion (Ginstling–Braunshtein equation)	$(1-2\alpha/3)-(1-\alpha)^{2/3}$
F1	Mampel unimolecular law	$-\ln(1-\alpha)$
R2	2D growth with constant interface velocity	$1-\ln(1-\alpha)^{1/2}$
R3	3D growth with constant interface velocity	$1-\ln(1-\alpha)^{1/3}$
A1	Branching nuclei: Prout Tompkins equation	$\ln[\alpha/1-\alpha]$
A2	Avarami–Erofeev (2D growth of existing nuclei with constant interface velocity)	$[-\ln(1-\alpha)]^{1/2}$
A3	Avarami–Erofeev (3D growth of existing nuclei with constant interface velocity)	$[-\ln(1-\alpha)]^{1/3}$

Decomposition reactions can be complex, with a number of different parameters influencing the kinetics (e.g., grain boundaries, defects, surface area, nucleation sites, and thermal conductivity). Generally, a single mechanism dominates, and this rate-limiting step can be determined from isothermal decomposition experiments. Many solid-state reaction mechanism models have been proposed including the diffusion, the geometrical contraction, the nucleation, and the reaction order models based on the different geometry of the particles and the different driving forces. Table 2 summarizes the most commonly used rate equations where α is the transformed fraction in time t with the reaction constant k. All the models, listed in Table 2, have been examined for the mea-

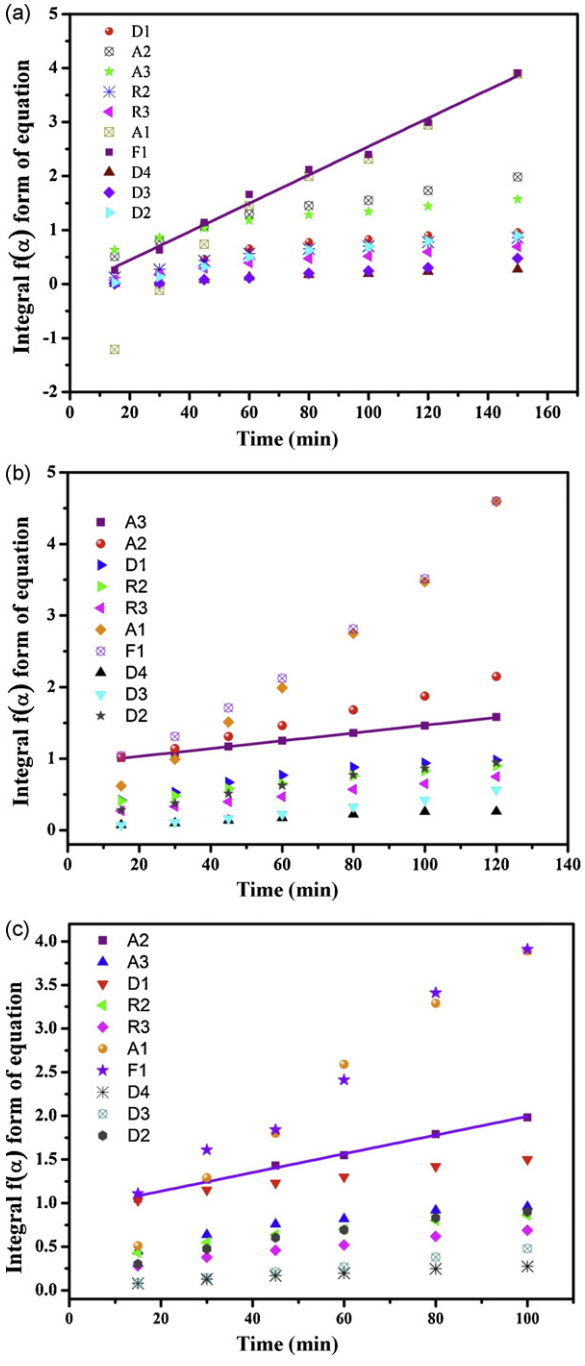

Fig. 5. The curves of different kinetic models applied to the isothermal dehydrogenation of $LiAlH_4$ + 2 mol% TiC at (a) 100 °C, (b) 115 °C, and (c) 125 °C. Illustration of kinetic models is given in Table 2.

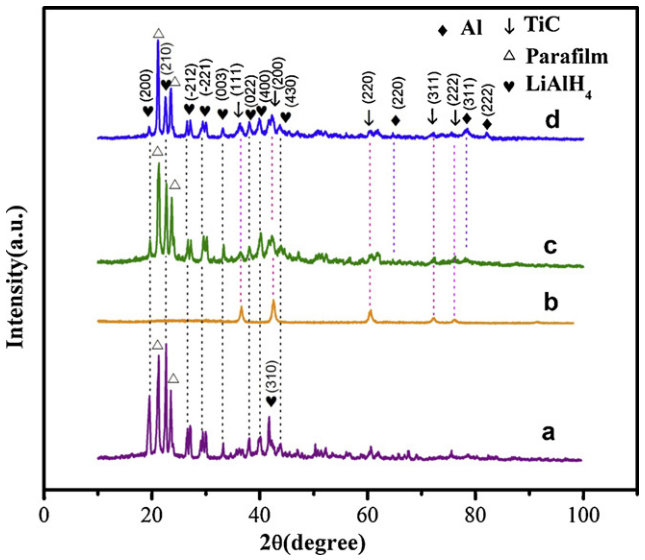

Fig. 6. X-ray diffraction spectra for (a) as-received $LiAlH_4$, (b) TiC nanopowder, (c) $LiAlH_4$ + 3 mol% TiC after ball-milling, and (d) $LiAlH_4$ + 5 mol% TiC after ball-milling.

surements achieved at 100 °C, 115 °C, and 125 °C. The results are presented in Fig. 5. In Fig. 5(a), the best correlation coefficient value ($R^2 > 0.99$) corresponds to the Mampel unimolecular law. Therefore, the desorption at 100 °C follows the Mampel unimolecular law formulated through random nucleation. In this approach, two-dimensional growth of randomly placed product nuclei in the form of edge-shaped planar circular discs proceeds simultaneously with the uncovering of surface gaseous species by desorption [47]. However, Fig. 5(b and c) clearly indicates that different mechanisms are controlling the rates at different temperatures of desorption. At higher desorption temperatures, the diffusion rate limitations predominate over random nucleation. It is evident in Fig. 5(b and c) that the hydrogen desorption at 115 °C and 125 °C correlates closely to the Avarami–Erofeev models represented by A3 and A2, respectively. These models involve two or three-dimensional growth with constant interface velocity.

Fig. 6 represents the powder X-ray diffraction patterns of as-received Li alanate, nano-sized TiC, and the Li alanate doped with 3 mol% and 5 mol% TiC nanopowders. The crystallite size is calculated by the Scherrer equation [$\beta = \lambda/(B\cos\theta)$, where β is the crystallite size, λ is the X-ray wavelength, and B is the full width at half maximum (FWHM)]. The FWHM values are corrected for instrumental broadening using warren's correction $B^2 = B_t{}^2 - B_i{}^2$, where B_t is the total broadening and B_i is the instrumental broadening. The Instrumental broadening is determined using the strongest peak from the XRD pattern of a silicon reference. The average crystallite size of as-received TiC is found to be 18 nm. In comparing the XRD profiles of pure and doped $LiAlH_4$, significant changes such as decrease in the relative intensities and increase in the full width at half maximum (FWHM) of XRD peaks corresponding to $LiAlH_4$ are observed. This phenomenon suggests the reduction of the average crystallite size of coarse $LiAlH_4$ matrix and the formation of large number of defects in the ball-milled composite. Some new weak peaks corresponding to Al phase appear in the XRD profiles of the doped samples. It is believed that the formation of Al is due to the first step decomposition reaction of $LiAlH_4$ during the ball-milling process, not the reaction of $LiAlH_4$ and TiC, because the diffraction peaks of any other reaction products are invisible. The absence of the diffraction peaks of the corresponding decomposition product Li_3AlH_6 is probably due to its small amount and weak X-ray scattering intensity.

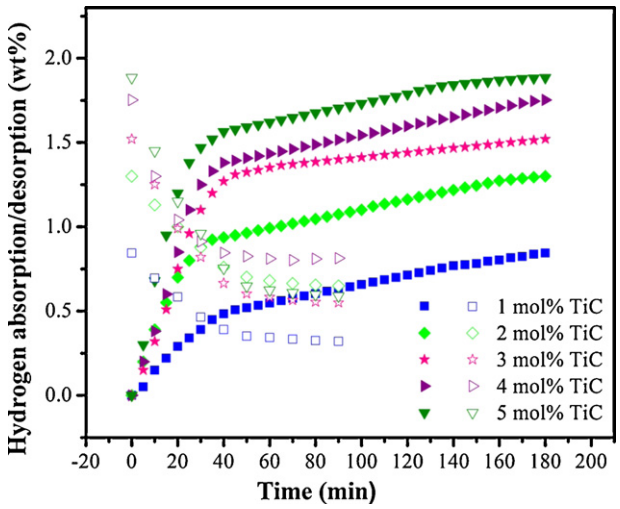

Fig. 7. Rehydrogenation (at 165 °C under 9.5 MPa) and subsequent dehydrogenation (at 165 °C) curves of $LiAlH_4$ doped with 1 mol%, 2 mol%, 3 mol%, 4 mol%, and 5 mol% TiC.

The diffractogramms of all the doped samples exhibit peaks at 35.9°, 41.7°, 60.4°, 72.3°, and 76.2° corresponding, respectively, to the (1 1 1), (2 0 0), (2 2 0), (3 1 1), and (2 2 2) reflections of f.c.c. TiC. This observation is rather curious since it is known that the existence of well-defined catalyst bearing phases, at low temperatures through X-ray diffraction, has not clearly been observed in TiF_3, $NiCl_2$, and NbF_5 doped $LiAlH_4$ systems [18,28,29]. However, the existence of catalyst bearing phases in the XRD spectra of sodium aluminum hydride catalyzed with TiC and TiN has already been proven [34,35]. In our investigation, the presence of X-ray diffraction peaks from TiC suggests that the TiC nanocrystalline particles/clusters are present with the $LiAlH_4$ matrix. Moreover, TiC is extremely hard and brittle, and it is thermodynamically more stable compound with a high Ti–C bonding strength. These features prevent TiC from reacting with $LiAlH_4$ to create any reaction products. Therefore, it is believed that TiC nanoparticles exist as stable and separate entities, and catalytically ameliorate the dehydrogenation performance of Li alanate.

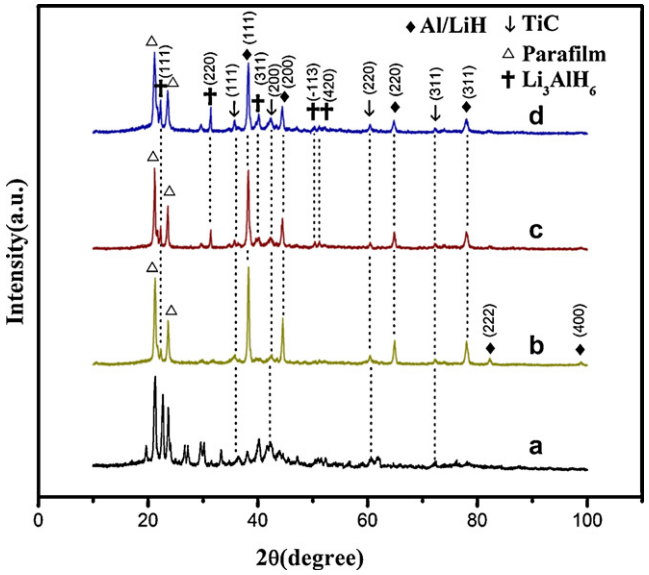

Fig. 8. X-ray diffraction spectra for (a) $LiAlH_4$ + 3 mol% TiC after ball-milling, (b) $LiAlH_4$ + 3 mol% TiC after first dehydrogenation at 125 °C for 3 h, (c) $LiAlH_4$ + 3 mol% TiC after first rehydrogenation, and (d) $LiAlH_4$ + 5 mol% TiC after first rehydrogenation.

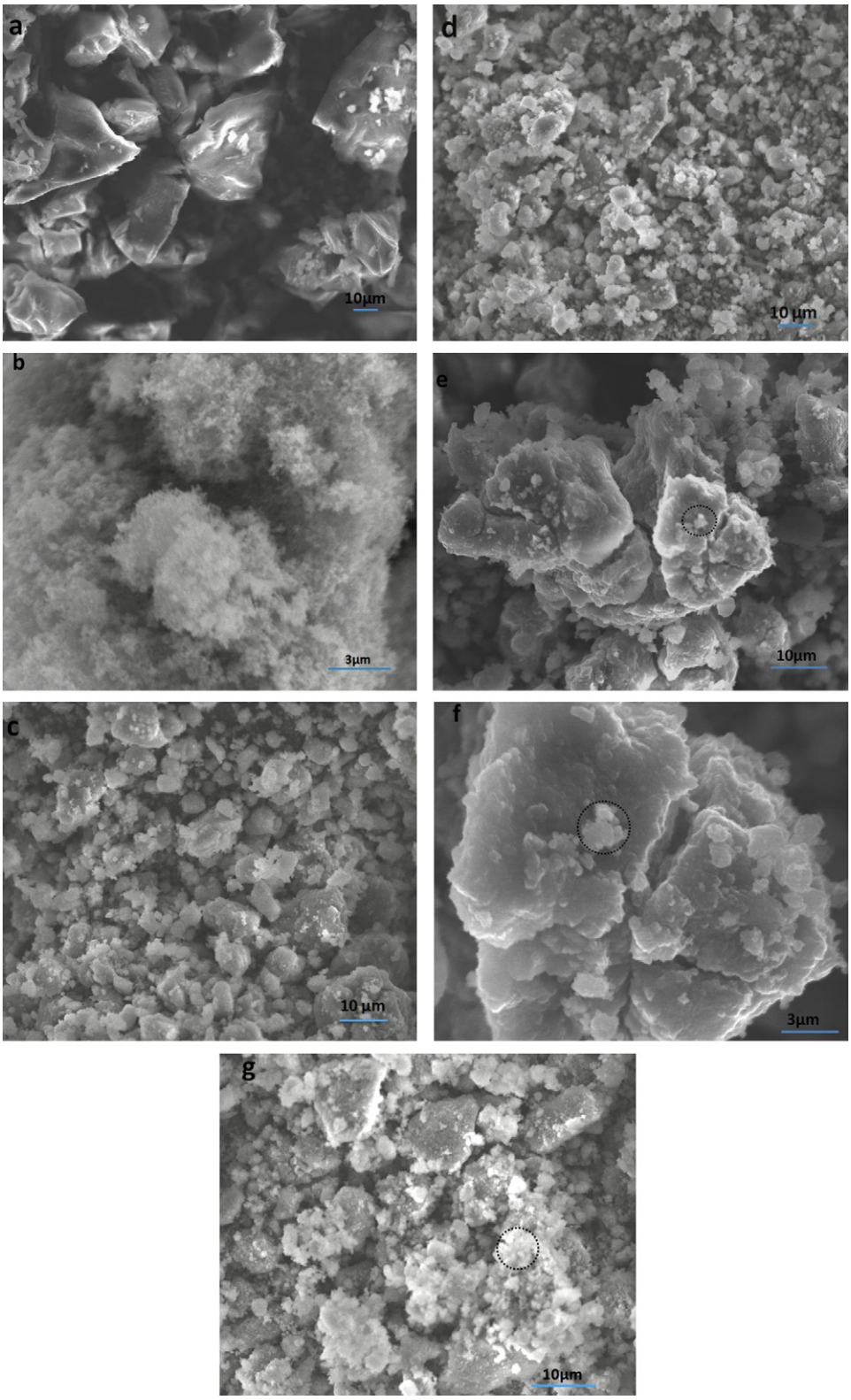

Fig. 9. Field emission scanning electron microscopy (FESEM) images of (a) as-received $LiAlH_4$, (b) nano-sized TiC powder, (c) $LiAlH_4$ + 3 mol% TiC after ball-milling, (d) $LiAlH_4$ + 5 mol% TiC after ball-milling, (e and f) $LiAlH_4$ + 3 mol% TiC after ball-milling at different magnifications, and (g) $LiAlH_4$ + 3 mol% TiC after first dehydrogenation.

Another important aspect of the hydrogen storage on alanates is the reversibility. It should be pointed out that the experiments carried out so far regarding the rehydrogenation of the Li alanate have not been quite successful [18,29]. After several trial runs of rehydrogenation experiments, it has been found that TiC:LiH:Al residues exhibit the rehydrogenation in the temperature range of 165–190 °C, and under a pressure of 9.5 MPa. Fig. 7 brings out the results of rehydrogenation followed by the subsequent desorption at 165 °C. After complete dehydrogenation of first two reactions, the samples have been rehydrogenated at 165 °C under 9.5 MPa.

The maximum rehydriding capacity is 1.9 wt.% for 5 mol% dopant. The amount of hydrogen absorption increases with an increase of the doping amount.

Fig. 8 shows the XRD patterns of the dehydrogenated and rehydrogenated samples. The weak diffraction peak of Li_3AlH_6 in the diffractogram b suggests that only small amount of Li_3AlH_6 is remained after dehydrogenation at 125 °C. The diffractograms c and d present the XRD profiles of the rehydrogenated samples following the rehydrogenation. The reduction in the intensity of Al/LiH peaks and the appearance of some new additional peaks of Li_3AlH_6 indicate that reaction (2) is partially reversible.

The FESEM images of as-received $LiAlH_4$, nano-sized TiC powder, and the ball-milled samples of $LiAlH_4$ doped with 3 and 5 mol% TiC nanopowders are shown in Fig. 9. As it can be seen, the sample of pure $LiAlH_4$ consists of large irregular shaped particles of up to ~40 μm extent. Fig. 9(c–f) exhibit representative FESEM pictures of the $LiAlH_4$ mechanically ball-milled with 3 mol% and 5 mol% of nano-sized TiC. Fig. 9(g) brings out the microstructural features of the doped material after complete dehydrogenation. The sample consists of segregated Al and LiH along with a porous surface matrix caused by the hydrogen release from the host structure. A comparison of Fig. 9(a) with Fig. 9(c–f) brings out two features. Firstly, the initial particles break into smaller particles of the sizes up to about one-fourth of the starting sample as also observed from the XRD profiles of the doped alanate. Secondly, the ball-milled particles show disordered surface features. This is vividly discernible in Fig. 9(e and f). Two important mechanical properties of TiC, which are relevant here, are its high hardness and the strength as typified by the Young's modulus of ~0.5 TPa. Thus, the TiC nanoparticles will act like grinding agent for the comparatively soft $LiAlH_4$ matrix. Wang et al. [48] have also shown that graphite acts as a micro-grinding agent through the formation of carbide species. Due to the rigorous ball-milling, the Ti carbide particles will undergo repeated collisions with $LiAlH_4$ matrix. Because of the nanosize and strength, the carbide particles may penetrate in alanate matrix. It is clear in Fig. 9(e and f) that the boundary division between catalyst and matrix becomes inconspicuous. After penetration, the TiC nanoparticles will produce deformed surface regions around them exhibiting many surface defects. The surface features as typified by the FESEM pictures, shown in Fig. 9(e and f), tallies with this envisaged scenario.

Fig. 10 shows the surface EDS spectra of TiC-doped $LiAlH_4$ composite before and after dehydrogenation. The EDS results of area circled in Fig. 9(e–g) confirm that the particle consists of Ti, C, Al and O. The exact quantitative analysis is not available owing to the difficulty in Li detection and the possible oxidation of the sample in the handling of sample preparation. However, the statistical analysis of EDS measurements over many places demonstrate that the variation of Ti contents is rather small, and the amount of Al contents is much higher than that of Ti contents at all the places of measurements.

IR spectroscopy has also been performed to study the influence of titanium carbide on $LiAlH_4$ vibrational spectrum. Active infrared vibrations of the Al–H bond of $LiAlH_4$ are found in two regions [39]: Al–H stretching modes (1760 cm^{-1} and 1610 cm^{-1}) and Li–Al–H bending modes (900 cm^{-1} and 830 cm^{-1}). With regard to Li_3AlH_6, it also exhibits two regions of active infrared vibration: Al–H stretching modes (1386 cm^{-1} and 1276 cm^{-1}) and Li–Al–H bending modes (1000 cm^{-1}, 950 cm^{-1}, and 850 cm^{-1}). Fig. 11(a) shows the FTIR spectra of as-received $LiAlH_4$. The bands with stretching modes are observed at 1770 cm^{-1} and 1610 cm^{-1}, while the bands with bending modes are found at 827 cm^{-1} and 900 cm^{-1}. With doping, all the four bands are still of $LiAlH_4$ and no band of Li_3AlH_6 is visible. However, in doped alanate, the Al–H stretching modes are shifted to higher frequencies (15 cm^{-1}). This shift may be attributed to the strain effects on the Al–H bond

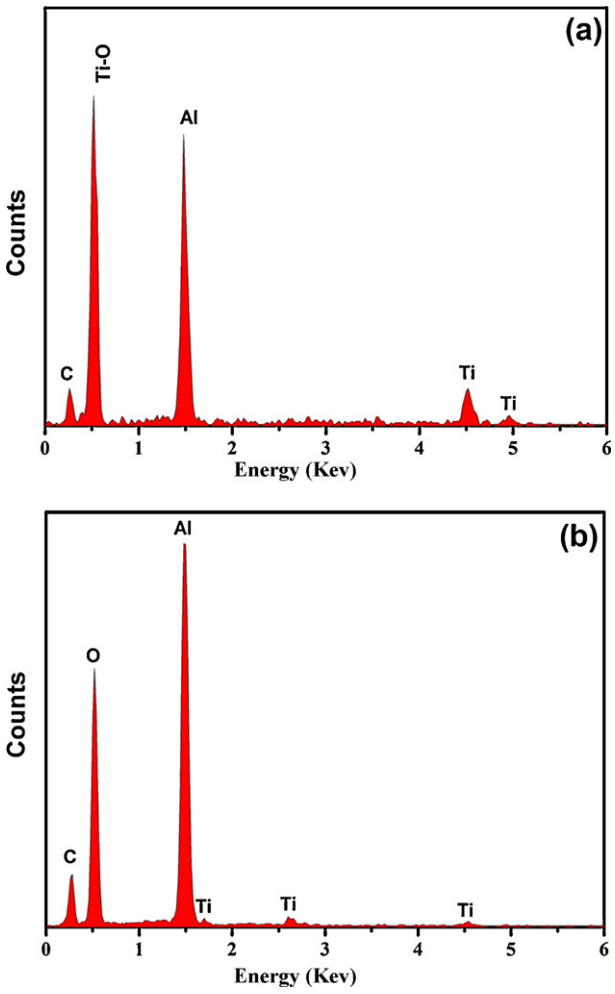

Fig. 10. Energy dispersive spectroscopy (EDS) results of (a) $LiAlH_4$ + 3 mol% TiC before dehydrogenation (area circled in Fig. 9(e and f)) and (b) $LiAlH_4$ + 3 mol% TiC after dehydrogenation (area circled in Fig. 9(g)).

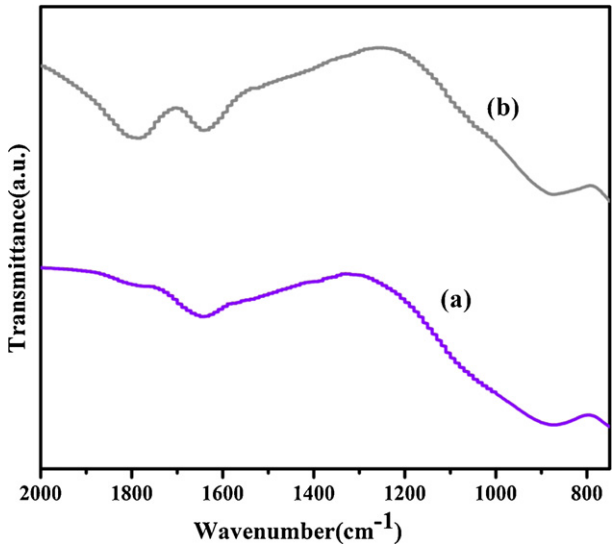

Fig. 11. FTIR spectra of as-received $LiAlH_4$ (a) and 2 mol% TiC-doped $LiAlH_4$ after ball-milling (b).

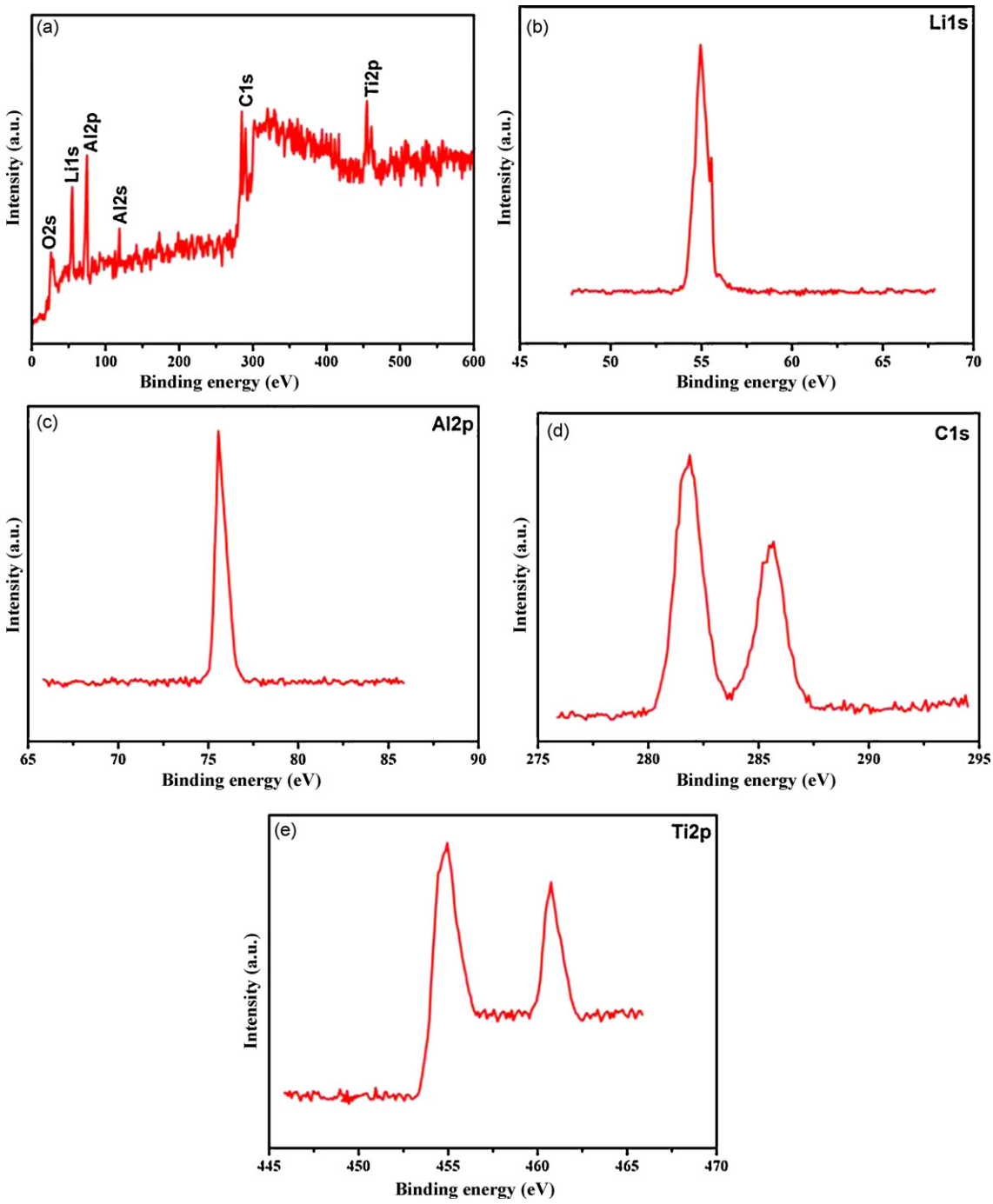

Fig. 12. (a) XPS survey spectrum of TiC-doped $LiAlH_4$. (b)–(e) Narrow scan XPS spectra of TiC-doped sample.

caused by the high pressures reached during the milling process [49].

Fig. 12 displays the XPS complete survey and narrow scan spectra of the ball-milled TiC-doped alanate sample. It is evident that the sample is consisted primarily of five elements, Li, Al. Ti, C and O. Fig. 12(a) shows the photoemission spectrum of Li1s, which occurs at about 54.95 eV. The binding energy of Li1s in LiCl lies in the range of 55.80–56.20 eV, which suggests that Li1s may correspond to the $LiAlH_4$ [50]. This result further testifies the absence of any reaction product during the ball-milling process. Two Al2p and Al2s peaks, located at 75.5 eV and 119.7 eV, are close to the Al peaks in $LiAlH_4$ at 75.6 eV and 199.90 eV [50]. The C1s and Ti2p XPS signals, correspond to the C and Ti in TiC, [50] present two doublets (Fig. 12(d and e)). Ti2P is composed of Ti2p3/2 and Ti2p1/2 with the binding energy of 454.7 eV and 460.6 eV, respectively. The C1s spectrum exhibits two peaks at 281.8 eV and 285.6 eV, respectively.

From above analysis, it can be surmised that nano particle TiC enhances the dehydriding/rehydriding performances of Li alanate by acting as a surface catalyst. The high-energy ball-milling of alanate with TiC nanopowder increases the surface defects and grain boundaries by reducing the particle and crystallite size of alanate. In the previous work by the authors [36], it is found that hydrogen absorption has a direct correlation with the defects in the nanostructures, and hydrogen desorption/absorption capability increases with increase in the vacancy defects in the nanostructures. The small values of enthalpies, acquired in this work for

the doped samples, may be attributed to the small grain size and large number of defects which can also upset the order in the alanate crystal structure and enable hydrogen to desorb more easily. As the energies of both reactants and products change going from bulk materials to nano-sized particles, the reaction thermodynamics will be affected by the size of the grains. Moreover, TiC {1 1 1} surface has been shown to be highly active for dissociative adsorption of hydrogen at room temperature [51]. Therefore, the additive TiC can have greater affinity for hydrogen compared to aluminium, thus destabilizing the Al–H bond. This feature facilitates the transfer of hydrogen from catalyst and alanate interface and thereby improves the desorption kinetics during dehydrogenation. Theoretical studies [52] also reveal dihydrogen binding and self-catalyzed hydrogenation for TiC nanocrystals. Ti atoms on the surface of the nanocarbides are capable of the dissociating the H_2 to form carbon hydrides. Therefore, during the rehydrogenation process, hydrogen molecule is easily dissociated into active hydrogen atoms on the catalyst surface, which are transferred through the hydrogen spillover provided by the TiC active species to react with the LiH and Al to form Li_3AlH_6.

4. Conclusions

The nano-sized TiC-doped Li alanate is shown to have greater and improved hydrogen performance in terms of storage capacity, kinetics, and initial temperature of decomposition, over the undoped Li alanate. Out of the various samples corresponding to $LiAlH_4$–x mol% TiC (x = 1, 2, 3, 4 and 5), it has been found that the sample with x = 2 mol% is the optimum material, which shows the highest desorption capacity leading to about 6.9 wt.% of H_2 by 188 °C (heating rate 4 °C min^{-1}). Addition of 2 mol% TiC nanopowder to lithium aluminum hydride results in the lowering of its decomposition temperature by 65 °C for the reaction (1) and about 50 °C for the reaction (2), respectively. Investigations reveal that the apparent activation energy as well as the enthalpy of dehydrogenation is considerably lowered by the addition of TiC nanopowder. $LiAlH_4$ doped with 5 mol% doping exhibits the maximum rehydrogenation capacity of 1.9 wt.% of hydrogen at 165 °C and 9.5 MPa. XRD, FESEM-EDS, FTIR, and XPS analyses show that nano TiC particles act as surface catalyst and remain stable during the milling process. Furthermore, it is believed that the addition of hard and brittle nano TiC to lithium aluminium hydrid increases the surface defects and grain boundaries by reducing the particle size, creating larger surface area for hydrogen to interact, thereby increasing the hydrogen capacity and decreasing the temperature for decomposition.

Acknowledgements

This work is financially supported by the University of Science and Technology Beijing (USTB). The authors also thank the Higher Education Commission (HEC) of Pakistan for the financial support to Rafi-ud-din.

References

[1] I.P. Jain, Pragya Jain, Ankur Jain, J. Alloys Compd. 503 (2010) 303–339.
[2] J. Yang, A. Sudik, C. Wolverton, D.J. Siegel, Chem. Soc. Rev. 39 (2010) 656–675.
[3] J. Yang, S. Hirano, Adv. Mater. 21 (2009) 3023–3028.
[4] B.H. Liu, Z.P. Li, J. Power Sources 187 (2009) 527–534.
[5] M. Zhu, M.Y. Chou, J. Alloys Compd. 479 (2009) 678–683.
[6] V. Iosub, T. Matsunaga, K. Tange, M. Ishikiriyama, Int. J. Hydrogen Energy 34 (2009) 906–912.
[7] L. George, S.K. Saxena, Int. J. Hydrogen Energy 35 (2010) 5454–5470.
[8] F. Zhan-Zhao, K. Xiang-Dong, W. Ping, L. Hai-Wen, O. Shin-Ichi, J. Alloys Compd. 491 (2010) L1–L4.
[9] S. Sartori, X. Qi, N. Eigen, J. Muller, T. Klassen, M. Dornheim, B.C. Hauback, Int. J. Hydrogen Energy 34 (2009) 4582–4586.
[10] T. Schmidt, L. Röntzsch, J. Alloys Compd. 496 (2009) L38–L40.
[11] Y. Jingkui, W. Xinhua, M. Jie, C. Lixin, P. Hongge, L. Shouquan, G. Hongwei, C. Changpin, J. Alloys Compd. 494 (2010) 58–61.
[12] C. Rugan, W. Xinhua Wang, C. Lixin, L. Shouquan, G. Hongwei, L. Yongquan, C. Changpin, J. Alloys Compd. 495 (2010) 17–22.
[13] M. Jianfeng, G. Zaiping, P.K. Chung, R. Abbas, G. Yanhui, Y. Xuebin, L. Huakun, J. Alloys Compd. 500 (2010) 200–205.
[14] J.F. Mao, X.B. Yu, Z.P. Guo, H.K. Liu, Z. Wu, J. Ni, J. Alloys Compd. 479 (2009) 619–623.
[15] N. Mehraj-ud-din, R. Sami-ullah, Z. Renju, S.S. Chang, H.W. Sang, K.R. Ae, N.S. Kee, J. Alloys Compd. 471 (2009) L16–L22.
[16] D.P.K. Gopi, M.S. Daniela, J. Phys. Chem. C 114 (2010) 8026–8031.
[17] M. Sterlin, L. Hudson, H. Raghubanshi, D. Pukazhselvan, O.N. Srivastava, Int. J. Hydrogen Energy 35 (2010) 2083–2090.
[18] L. Shu-Sheng, et al., Int. J. Hydrogen Energy 34 (2009) 8079–8085.
[19] Z. Xueping, L. Ping, X. Haga, I.S. Humail, Y. Zhang, W. Guoqing, J. Univ. Sci. Technol. Beijing 15 (2008) 786–790.
[20] Z. Xueping, L. Shenglin, J. Alloys Compd. 481 (2009) 761–763.
[21] Y. Kojima, Y. Kawai, M. Matsumoto, T. Haga, J. Alloys Compd. 462 (2008) 275–278.
[22] D. Blanchard, H.W. Brinks, B.C. Hauback, P. Norby, J. Muller, J. Alloys Compd. 404–406 (2005) 743–747.
[23] J. Chen, N. Kuriyama, Q. Xu, H.T. Takeshita, T. Sakai, J. Phys. Chem. B 105 (2001) 11214–11220.
[24] Z. Xueping, L. Ping, I.S. Humail, A. Fuqiang, W. Guoqing, Q. Xuanhui, Int. J. Hydrogen Energy 32 (2007) 4957–4960.
[25] J.R. Ares Fernandez, F. Aguey-Zinsou, M. Elsaesser, X.Z. Ma, M. Dornheim, T. Klassen, R. Bormann, Int. J. Hydrogen Energy 32 (2007) 1033–1040.
[26] Z. Xueping, L. Ping, A. Fuqiang, W. Guoqing, Q. Xuanhui, Rare Met. Mater. Eng. 37 (3) (2008) 400–403.
[27] N. Mehraj-ud-din, et al., Int. J. Hydrogen Energy 34 (2009) 8937–8943.
[28] T. Sun, C.K. Huang, H. Wang, L.X. Sun, M. Zhu, Int. J. Hydrogen Energy 33 (2008) 6216–6221.
[29] M. Ismail, Y. Zhao, X.B. Yu, S.X. Dou, Int. J. Hydrogen Energy 35 (2010) 2361–2367.
[30] L.H. Kumar, B. Viswanathan, S.S. Murthy, Int. J. Hydrogen Energy 33 (2008) 366–373.
[31] S. Srinivasan, D. Escobar, M. Jurczyk, Y. Goswami, E. Stefanakos, J. Alloys Compd. 462 (2008) 294–302.
[32] P. Choudhury, S.S. Srinivasan, V.R. Bhethanabotla, Y. Goswami, K. McGrathd, E.K. Stefanakos, Int. J. Hydrogen Energy 34 (2009) 6325–6334.
[33] B. Bogdanović, M. Felderhoff, S. Kaskel, A. Pommerin, K. Schlichte, F. Schüth, Adv. Mater. 15 (2003) 1012–1015.
[34] K.W. Ji, et al., J. Power Sources 192 (2009) 582–587.
[35] X. Xuezhang, et al., J. Phys. Chem. C 113 (2009) 20745–20751.
[36] A. Mashkoor, Rafi-ud-Din, P. Caofeng, Z. Jing, J. Phys. Chem. C 114 (2010) 2560–2565.
[37] V.W. Andrew, et al., Int. J. Hydrogen Energy 34 (2009) 2333–2339.
[38] A. Andreasen, J. Alloys Compd. 419 (1–2) (2006) 40–44.
[39] J.R. Ares, et al., Mater. Res. Bull. 43 (2008) 1263–1275.
[40] S.-I. Orimo, Y. Nakamori, J.R. Eliseo, A. Züttel, C.M. Jensen, Chem. Rev. 107 (2007) 1432–4111.
[41] O.M. Lþvvik, Phys. Rev. B 69 (2004) 134117.
[42] H. Kissinger, Anal. Chem. 29 (1957) 1702–1706.
[43] A. Andreasen, T. Vegge, A.S. Pedersen, J. Solid State Chem. 178 (2005) 3672–3678.
[44] R.A. Varin, T. Czujko, Z.S. Wronski, Nanomaterials for Solid State Hydrogen Storage, Springer Science+Business Media, New York, NY, 2009.
[45] M. McCarty Jr., J.N. Maycock, V.R. Pai Verneker, J. Phys. Chem. 72 (1968) 4009–4014.
[46] R.A. Varin, L. Zbroniec, J. Alloys Compd. (2010), doi:10.1016/j.jallcom.2010.05.059.
[47] H. Tanaka, N. Koga, J. Chem. Ed. 72 (3) (1995) 251.
[48] J. Wang, et al., J. Alloys Compd. 395 (2005) 252–262.
[49] A.V. Talyzin, B. Sundqvist, Phys. Rev. B 70 (2004) 180101.
[50] http://srdata.nist.gov/xpx/.
[51] C. Oshima, M. Aono, S.Y. Otani, Ishizawa, Solid State Commun. 18 (1983) 911–913.
[52] Y. Zhao, C.D. Anne, K. Yong-Hyun, J.H. Michael, S.B. Zhang, Chem. Phys. Lett. 425 (2006) 273–277.